PHYSICAL REVIEW E **93**, 063004 (2016)

Nucleation of plasticity in nanoparticle collisions

Emmanuel N. Millán,[1] Diego R. Tramontina,[1,2] Herbert M. Urbassek,[3,*] and Eduardo M. Bringa[1]
[1]*CONICET and Facultad de Ciencias Exactas y Naturales, Universidad Nacional de Cuyo, Mendoza, 5500 Argentina*
[2]*Instituto de Bioingeniería, Universidad de Mendoza, Mendoza, M5502BZ Argentina*
[3]*Physics Department and Research Center OPTIMAS, University Kaiserslautern, Erwin-Schrödinger-Straße, D-67663 Kaiserslautern, Germany*

(Received 5 February 2016; published 27 June 2016)

While at small collision velocities collisions of nanoparticles (NPs) are elastic, they become plastic at higher velocities. We study the elastic-plastic threshold and the onset of plasticity using molecular dynamics simulation for a Lennard-Jones material. The reasons behind the $R^{-2/3}$ increase of the threshold velocity for small NP radii R found recently are discussed. At the threshold, NP orientation strongly influences the generation of plasticity, and averaging over many orientations is required to predict the critical velocity for dislocation generation. The onset of plasticity is governed by the generation of isolated stacking faults and nanotwins spanning the entire NP. At higher velocities, the fraction of defects becomes proportional to the total number of atoms in the NP.

DOI: 10.1103/PhysRevE.93.063004

I. INTRODUCTION

Collisions of spherical nanoparticles (NPs) are ubiquitous in physics as well as in applications ranging from engineering to astrophysics [1–6]. This topic is central to the field of granular mechanics, which studies the behavior of ensembles of grains interacting with each other [7,8]. However, even the interaction of two identical spherical particles still poses fundamental problems. Macroscopic collision models use interparticle adhesion, elastic repulsive forces, and viscoelastic damping to describe central collisions at small velocities [9]. For noncentral collisions, a number of various friction forces have to be introduced [10]. At higher collision velocities, the plastic deformation of the colliding spheres forms an increasingly important channel for energy dissipation which strongly influences the outcome of the collision.

It is therefore decisive to characterize the threshold velocity v_c, termed the "critical velocity," above which plasticity starts to play a role: the elastic-plastic threshold. Early models assume the critical velocity to be independent of the NP size [11–14], but it was found recently by molecular dynamics (MD) simulation that $v_c \propto R^{-2/3}$, where R is the NP radius [15].

In recent years the elastic-plastic threshold could also be investigated by uniaxial compression experiments performed on NPs under well-controlled conditions, in which a continuously increasing pressure enforces plastic yielding of the material. These experiments are quasistatic in the sense that the compression velocity is orders of magnitude smaller than that in collision experiments. They have been performed on nanoclusters [16,17] and nanopillars [18] and also in adhesive contacts [19]. While NP collisions occur under high strain rates, controlled experiments are more easily performed for quasistatic compression experiments. Here, Han *et al.* [20] show that indeed small (<200 nm) Fe NPs may be defect free and show ideal strength; this may serve as a motivation to use crystalline, defect-free NPs for our study. Mordehai *et al.* [21] studied dislocation nucleation in Au NPs under quasistatic compression. Experiments performed on $R = 100$–500 nm sized NPs showed a decrease of the critical stress for the onset of plastic deformation as a power law, $\sigma_c \propto R^{-n}$ with $n = 0.77 \pm 0.16$.

In this paper we study the onset of plasticity in NP collisions using MD simulation. We use the Lennard-Jones (LJ) interaction potential as a generic and well-understood potential. LJ has been used in previous studies of material failure, both fracture and under shock loading [22–27]. Zimmerman *et al.* [28] showed that it describes well the plastic deformation behavior of fcc EAM solids. In particular, it reproduces well the unstable stacking fault energy of these materials. We study the dependence of the plasticity generated on NP size and collision velocity. We show that a careful consideration of collision statistics (averaging over orientations) is necessary at the threshold.

The shape and structure of NPs may be complex and depend on their growth or production process [29]. In addition, depending on the material, besides the crystalline phase, also the amorphous phase may contribute to its structure. Even if the structure is crystalline, defects such as grain or twin boundaries may be present. For instance, in metallic NPs prepared by inert gas condensation, multiply twinned structures have been found and lead to peculiar mechanical properties such as increased ductility and tensile strength [18,30]. In this paper, we take the approach to study single-crystalline fcc particles with a nonfaceted spherically shaped surface, since already such a simplified structure gives rise to a considerable richness in plastic-deformation behavior. Future investigations might study the influence of pre-existing defects in these NPs—such as the well-known multiply twinned NPs—of an amorphous phase, and of faceted surfaces.

II. METHOD

We employ a generic interatomic interaction potential, the LJ potential, which has been frequently used in the past to model NP collisions [31–35]. The plastic behavior of LJ solids has been thoroughly studied, in particular under shock loading and the dislocation activity in LJ solids has been found to be typical of that of fcc crystals [25–27]. LJ potentials are

---

[*] urbassek@rhrk.uni-kl.de; http://www.physik.uni-kl.de/urbassek/

TABLE I. LJ parameters, ϵ and σ, and mass, m, for Ar [36,37] and Au [38]. LJ units for velocity, $\bar{v} = \sqrt{\epsilon/m}$, time $\bar{t} = \sigma\sqrt{m/\epsilon}$, temperature, $\bar{T} = \epsilon/k_B$, and pressure, $\bar{p} = \epsilon/\sigma^3$, where k_B is Boltzmann's constant.

	ϵ (meV)	σ (Å)	m (amu)	$\bar{v}$ (m/s)	$\bar{t}$ (ps)	$\bar{T}$ (K)	$\bar{p}$ (MPa)
Ar	10.32	3.41	39.95	158	2.16	119.8	41.6
Au	441	2.637	196.97	464	0.568	5123	3848

characterized by their well depth ϵ and the length parameter σ. The potential is cut off at $r_c = 2.5\sigma$. Data will be reported in reduced LJ units. Table I specifies these units for two materials: Ar and Au.

The NPs are built by carving spheres of radius R from a perfect fcc structure. They are energy minimized to relax their structure and then equilibrated to a final temperature of $T = 0.1$, while keeping the total angular and linear momentum zero. We note that we tested the effect of additional relaxation steps in the initial configuration, but the final outcome did not significantly differ with respect to plasticity nucleation. After relaxation, the NPs exhibit some roughness on an atomistic scale, in particular the smaller ones. Such surface roughness might provide nucleation sites for plasticity, but the averaging over many collision sites tends to minimize this effect.

The number of atoms, N, in a spherical NP is connected to its radius by $R = 0.607\times N^{1/3}$ or $N = 4.47\times R^3$. We study NPs in the range of $N = 10^3$ to 10^6, equivalent to $R = 6.1$ to 61. The relative orientation between the colliding NPs has been varied; the quantitative results shown are averages of up to 1000 orientations.

The molecular dynamics code LAMMPS [39] is used to perform the simulations. We employ a time step of 0.001. The simulations are carried out at in the constant energy ensemble for an initial temperature of $T = 0.1$. We pursue the simulations for a time of at least 2×10^5 LJ units. The generated defects are tracked using the dislocation extraction algorithm (DXA) [40,41] and the crystal analysis tool (CAT) [42]. Visual molecular dynamics (VMD) [43] and OVITO [44] are used to view the simulation results.

For comparison with macroscopic models, a number of materials parameters for LJ materials are relevant. Quesnel *et al.* [45] calculated for a LJ fcc solid a density of $\rho = 1.08485$. In the same paper they recommend isotropic values for the elastic properties—as determined from an appropriate orientation averaging over the elastic constants. Young's modulus is $E = 100$ and the Poisson ratio amounts to $\nu = 0.25$. This results in an indentation modulus of $E_{\text{ind}} = E/(1-\nu^2) = 107$. The shear modulus is $G = 40$ and the bulk modulus is $K = 67$. The longitudinal velocity of sound in the isotropic case is $c_l = \sqrt{(K+4G/3)/\rho} = 10.52$. The surface energy is $\gamma = 2.3$ [46].

III. RESULTS

A. Time evolution

We first discuss the time evolution of the collision for two exemplary cases. In Fig. 1 the dynamics of the collision of two NPs of radius $R = 13.2$ ($N = 10^4$) colliding with velocity $v = 0.5$ is displayed. Figure 1(a) shows the evolution of the pressure in the contact zone during the collision. The contact area has a maximum radius of roughly $r = 5$ in this case; so we average the pressure in a sphere of radius $r = 5$ centered on the collision point. The normal pressure component in the direction of the collision axis (i.e., connecting the two centers of the NPs), p_{zz}, is shown together with the shear stress, which is obtained as the difference of p_{zz} and the average normal pressure in perpendicular direction,

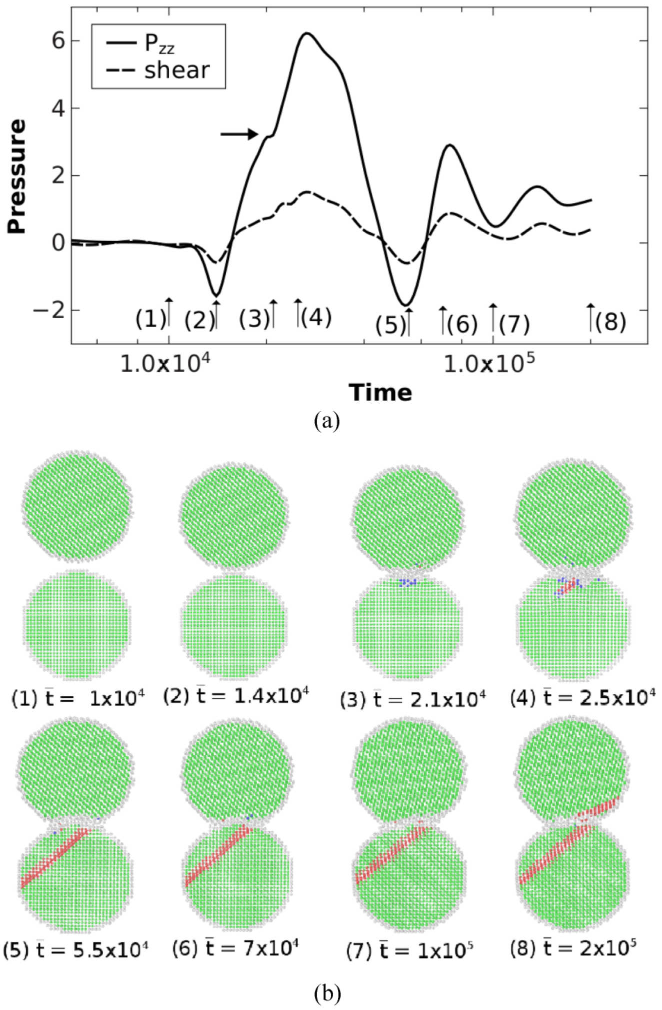

(a)

(b)

FIG. 1. Temporal evolution of the collision of two NPs of radius $R = 13.2$ ($N = 10^4$) colliding with velocity $v = 0.5$. (a) Normal pressure, p_{zz}, and shear pressure, p_{shear}, Eq. (1), averaged over a sphere of radius $r = 5$ over the contact zone. The arrow highlights the onset of plasticity. (b) Snapshots showing the nucleation and evolution of plasticity in the collision. Green: fcc; red: planar defects, gray: surface atoms. Numbers correspond to those in subfigure (a).

$$p_{\text{shear}} = p_{zz} - (p_{xx} + p_{yy})/2\,. \qquad (1)$$

Upon approaching, the attractive forces lead to a tensile stress; when the two NPs start overlapping, the pressure grows and assumes large values, up to $p_{zz} = 6$. At $t = 21\times 10^3$, dislocations are nucleated at a pressure of $p_{zz} = 3.1$; the shear stress here amounts to $p_{\text{shear}} = 0.75$. We note that the pressure in the contact zone area is highly inhomogeneous and reaches maximum values of ∼15. After the onset of plasticity, the pressure reaches a small plateau during dislocation nucleation, since the yield process relieves stress. However, since the collision continues the pressure keeps increasing after dislocation emission. Upon reversal of the NP velocities, the pressure is reduced again. A series of oscillations after the end of the collision indicates the excitation of large-wavelength vibrations in the spheres that help dissipate the collision energy in the fused NPs.

To put the pressures into perspective, we note that in bulk LJ material, dislocations require a pressure of 24.5 to nucleate [26]; this characterizes the Hugoniot elastic limit (HEL) of a LJ crystal. However, in that same study it was found that the introduction of defects (a void with radius r) in the crystal decreases the HEL dramatically. The HEL reaches 20% of the original value ($p_{zz} = 4.9$) for a void of radius $r = 5$ and continues dropping for larger voids. The void acts as a nucleation site for dislocation nucleation. This situation is comparable to the emergence of nanoplasticity in our system, where the highly disordered contact area assists the nucleation.

Figure 1(b) provides snapshots showing the generation of dislocations. As this collision is at the elastic-plastic threshold, the pressure is barely sufficient to generate a few isolated dislocations. Note that here and in the following we shall denote by planar defects both the stacking fault (SF) planes and the twin boundaries of nanotwinned regions. They are typically formed by the emission of a partial dislocation which runs through the NP until it is absorbed at the surface at the opposite end. Due to the small SF energy, these large SF platelets may form without a trailing partial dislocation following the leading one. We note that SFs are characterized in our plots by the occurrence of two neighboring $\{111\}$ planes, nanotwin boundaries by one $\{111\}$ plane.

The first plastic activity is seen at a time of around $t = 21\times10^3$; a dislocation starts growing into the lower NP and has penetrated it fully at $t = 55\times10^3$. Quite late, at $t = 200\times10^3$, a second dislocation has also appeared in the upper NP. Note that dislocations nucleate directly at the contact area. First they only nucleate in one of the NPs, even though both NPs are identical. This is due to the different orientations of both spheres with respect to each other; the critical resolved shear stress to activate dislocation glide on a $\{111\}$ plane is reached only in one of them.

In Fig. 2, we display the dynamics of a second collision event, for two NPs of radius $R = 60.7$ ($N = 10^6$) colliding with velocity $v = 0.5$. This case is far above the elastic-plastic threshold. Plastic activity starts here somewhat later, at $t = 27\times10^3$, again followed by a plateau in the compressive pressure. Note that in this case, the collision does not show the pressure oscillations that characterized the collision of the smaller NPs, Fig. 1. This is due to the pronounced plastic activity which dissipates energy.

Initially, at time $t = 30\times10^3$, two dislocations are nucleated at the contact interface in the lower NP. The two dislocations intersect after which their motion is retarded. At time $t = 70\times10^3$, beyond the pressure maximum, a burst of dislocations is emitted from the contact area parallel to the first ones in the lower NP and defines nanotwin regions there. At this time also dislocation emission into the upper NP becomes possible. Note that dislocations now also are emitted from the boundary of the upper NP, showing the heterogeneous nature of dislocation nucleation. After the end of the collision the number of defects has again been reduced—in particular in the upper NP—since the pressure has relaxed. By the action of the various glide systems activated the contact interface has become considerably rough. The series of SFs in the upper NP enclose a nanotwin region.

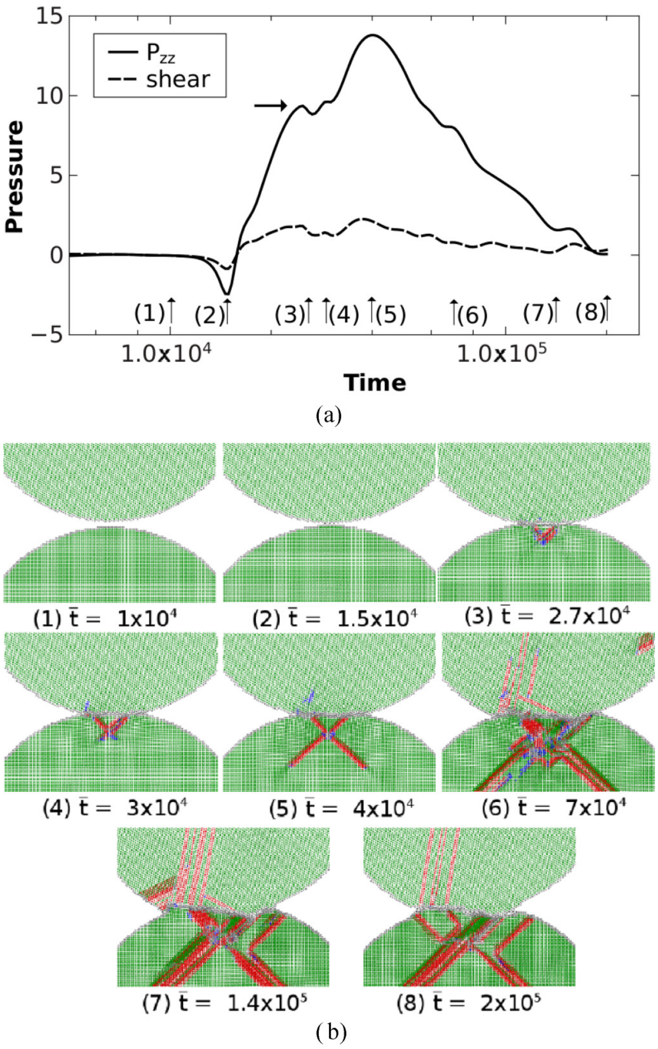

FIG. 2. Analogous to Fig. 1 but for two NPs of radius $R = 60.7$ ($N = 10^6$) colliding with velocity $v = 0.5$.

For further use we also display the evolution of the contact radius a for the two events studied in Fig. 3. It is calculated from the MD data of the N_0 interface atoms with positions $\mathbf{r}_i$ and center-of-mass $\bar{\mathbf{r}}$ via [47,48]

$$a = \sqrt{\frac{2}{N_0}\sum_{i=1}^{N_0}(\mathbf{r}_i - \bar{\mathbf{r}})^2}\,. \qquad (2)$$

For the smaller NPs, the oscillatory nature of the collision visible in the pressure, Fig. 1, is also reflected in the contact radius. The contact radius of the larger NPs shows a constant increase during the time when the pressure is compressive, up to $t = 4\times10^4$. The subsequent decrease in the contact area is caused by the relaxation and reorganization of the interface caused by pressure relaxation and dislocation reactions; it is also directly visible in Fig. 2(b).

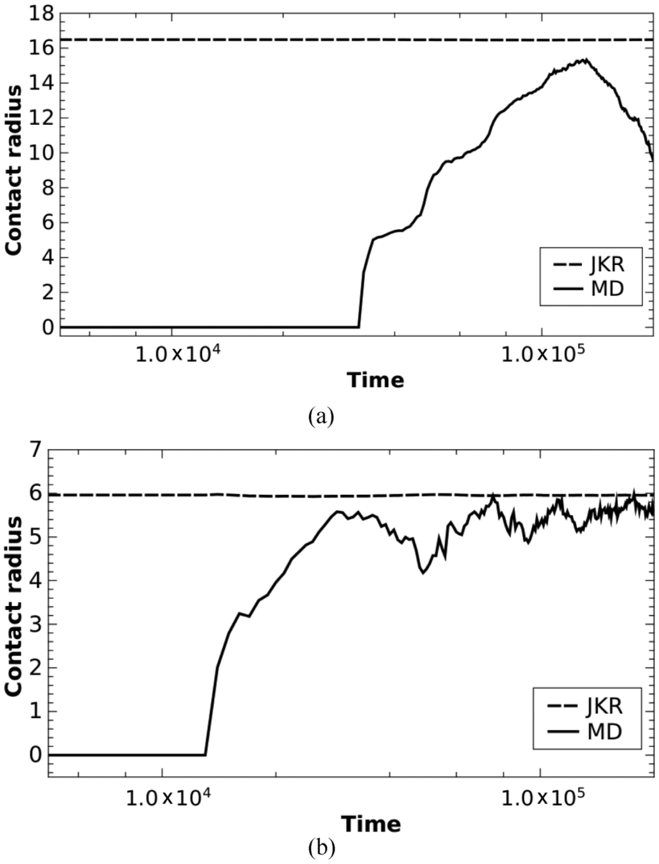

(a)

(b)

FIG. 3. Temporal evolution of the contact radius a during the collision of two NPs of radius (a) $R = 13.2$ and (b) $R = 60.7$ colliding with velocity $v = 0.5$. The JKR estimate, Eq. (4), is indicated.

We include in Fig. 3 the macroscopic estimate of the contact radius provided by the Johnson-Kendall-Roberts (JKR) model [12,49]. This model is designed for large compliant particles with short-ranged attraction and is believed to describe LJ systems well [33,47]. For vanishing external force it is

$$a = \left(\frac{9\pi w}{E_{\text{ind}}} R^2\right)^{1/3}, \tag{3}$$

where $w = 2\gamma$ is the work of adhesion, γ is the surface energy, $E_{\text{ind}} = E/(1-\nu^2)$ is the indentation modulus, and E and ν are Young's modulus and Poisson ratio. For a LJ material, Eq. (3) yields

$$a = (1.22R^2)^{1/3}. \tag{4}$$

Figure 3 demonstrates that the JKR estimate predicts the maximum contact radius quite well. This finding is in agreement with the results of Luan and Robbins [50,51], who studied the validity of JKR for describing the quasistatic interaction of tips with surfaces using the LJ potential. They showed that the MD results fulfill well the $a \propto R^{2/3}$ prediction of JKR.

B. Plasticity at the threshold

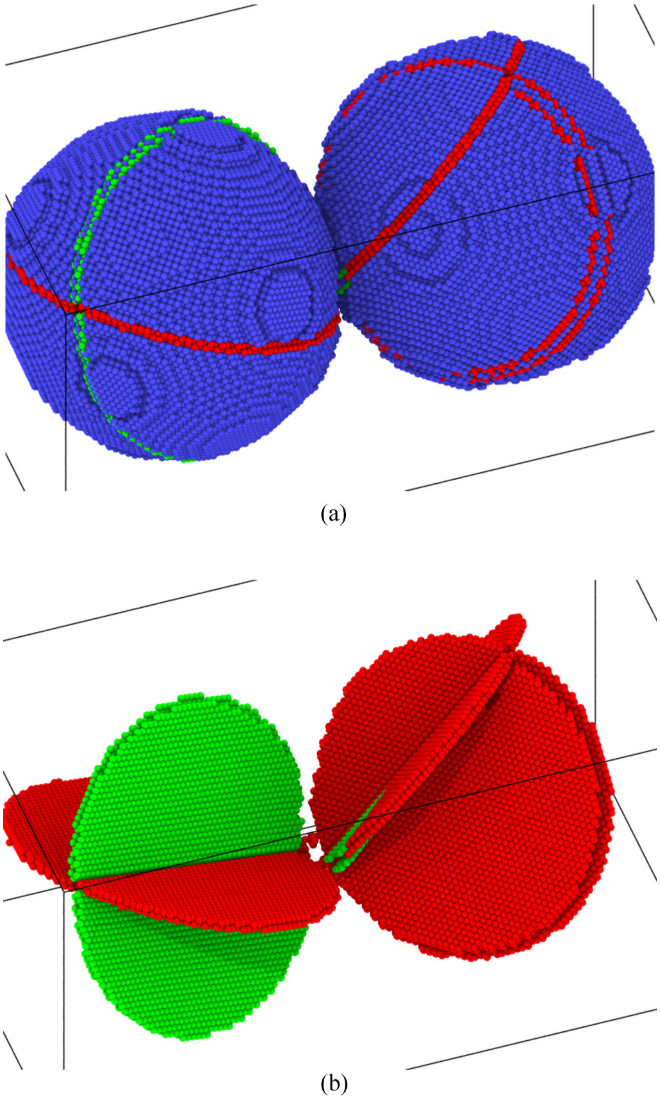

(a)

(b)

FIG. 4. Typical defects generated above the critical velocity. Data taken for two NPs of radius $R = 28.7$, $N = 10^5$ colliding with velocity $v = 0.5$. Blue: Undisturbed lattice; red: SF; green: twins. (a) View on the collided system; (b) undisturbed lattice atoms removed.

Figure 4 gives a view on the plasticity developing at velocities slightly above the critical velocity. The large stress in the contact area leads to partial dislocations traveling rapidly through the material. When they reach the opposite surface of the NP, they are absorbed, leaving behind the SF. The generation of SFs is characteristic of the plasticity of the NPs studied here. If several SFs are produced in consecutive planes, then a nanotwin is formed, such as that seen in Fig. 4(b). For certain events around v_c, we observe production of transient SFs which do not reach the opposite surface and can be reabsorbed leaving defect-free grains at the end of the simulation, as noted before [52,53].

While below the critical velocity (not shown here), only embryonic features are seen—amorphous or platelike strongly constrained structures—above v_c full SF platelets spanning the entire respective NP have formed. This demonstrates that already slightly above v_c plasticity is characterized by the formation of volume-spanning planar defects. Dislocations generally nucleate directly at the contact area; from there they expand until they span the entire NP.

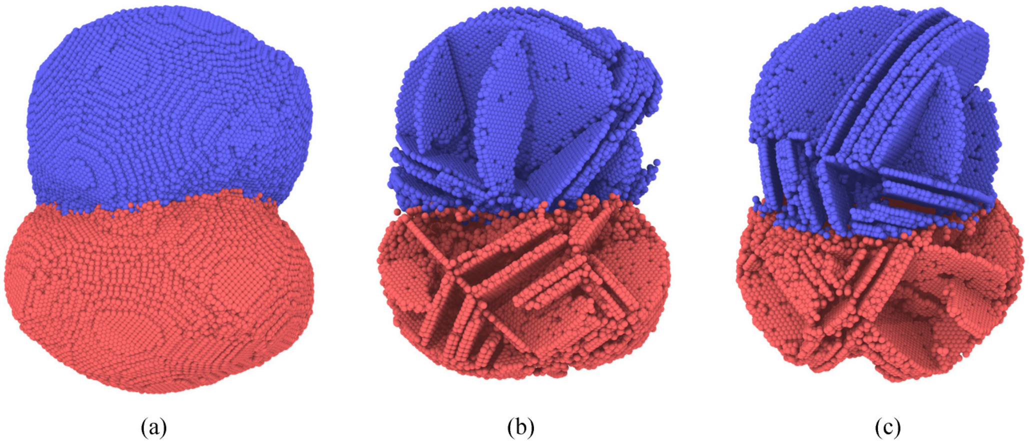
(a) (b) (c)

FIG. 5. Typical example of a complex defect structure obtained far above the critical velocity. Data taken for two NPs of radius $R = 28.7$, $N = 10^5$, colliding with velocity $v = 2$. (a) View on the collided NPs. (b) Intermediate damage structure; note the occurrence of a full dislocation in the upper NP. (c) Final damage structure. Colors distinguish material of the two NPs.

As a consequence of the collision, the temperature in the NPs is changed. We checked the temperature increase in the NPs after the collision in the velocity range around the critical velocity. For all NP sizes the temperature increase caused by the collision is less than 0.005; compared to the initial temperature of 0.1 this increase is negligible.

C. Plasticity far above the threshold

In Fig. 5 we display the defect structure in a high-velocity collision, far above the elastic-plastic threshold. The two NPs merge and are considerably deformed; note the clear slip bands noticeable in particular in the upper NP in Fig. 5(a). The defect structures in the middle of the collision, Fig. 5(b), and at its end, Fig. 5(c), are characterized by planar defects. These are as a rule SFs extending throughout the NP, but also several nanotwin boundaries are observed. Note the dense packing of planar defects. While several glide planes have been activated, the SFs run mainly parallel to each other. In this way, a volume filling defect density is reached. Note that no amorphized regions are seen, since slip is an easy way to relax pressure out of the highly activated collision zone.

SFs are produced when one partial dislocation is emitted from the contact area and expands throughout the NP, reaching the opposite boundary before a trailing partial dislocation is emitted. At high-velocity collisions it is possible that the stress produced in the contact zone is high enough that also a trailing partial is emitted and thus a full dislocation runs through the NP. In the intermediate plot, Fig. 5(b), such a full dislocation is visualized while it is still running through the NP, before its absorption on the NP surface. Its width amounts to 10–14 in LJ units; note that this constitutes a lower bound since the leading partial has already encountered the surface.

The width, $w_{\rm SF}$, of a fully dissociated dislocation depends on the shear modulus G, the Burgers vector length b, and the stacking fault energy $\gamma_{\rm SF}$ as [54,55]

$$w_{\rm SF} = \frac{Gb^2}{2\pi\gamma_{\rm SF}}. \qquad (5)$$

The stable stacking fault energy is small; Ziegenhain *et al.* [56] give a value of 0.024 in LJ units and Kogure *et al.* [57] a value of 0.052 for another LJ cut-off radius. Hence dislocations show a broad stacking fault ribbon between leading and trailing partial. This allows also partials to easily cross the NP leaving behind a SF. From Eq. (5) we hence obtain a width of $w_{\rm SF} = 316$ (146) for $\gamma_{\rm SF} = 0.024$ (0.052). These excessively large values hold in equilibrium in bulk material. Under the large stresses prevalent in the contact zone the trailing partial is emitted earlier and the SF width is shortened.

We thus conclude that partial dislocations and even full dislocations play a dominant role in NP plasticity, while amorphization is not found. This finding is at variance with previous arguments that dislocation plasticity plays no role in NP collisions due to the limited space and time scales [58].

D. Bouncing

We note that we occasionally see bouncing of the two NPs. This is in agreement with the systematic study of Kalweit and Drikakis [31], who investigate the bouncing regime—called “stretching separation mode” by these authors—for small NPs as a function of collision velocity and impact parameter. Bouncing occurs around v_c, when the velocity is high enough to allow the 2 NPs to separate again after the collision but small enough that plasticity does not yet dominate energy dissipation [31,33]. Figure 6 shows an example of such an event. We observe that some mass transfer occurred at the contact area from the upper to the lower NP. This grain mixing is caused by the fact that the strong adhesion between the two grains, consisting of the same material, has led to a welding of the two NPs at the contact area; on break-up atoms feel equally bound to either of the NPs. We note that in dedicated studies of NP bouncing, some authors judiciously choose a purely repulsive interaction between the NPs [35] in order to enhance the bouncing effect.

E. Dependence on impact parameter

NP collisions are characterized by their impact parameter b, which ranges between 0 and $2R$; central (collinear) collisions are characterized by $b = 0$, while (peripheral) glancing

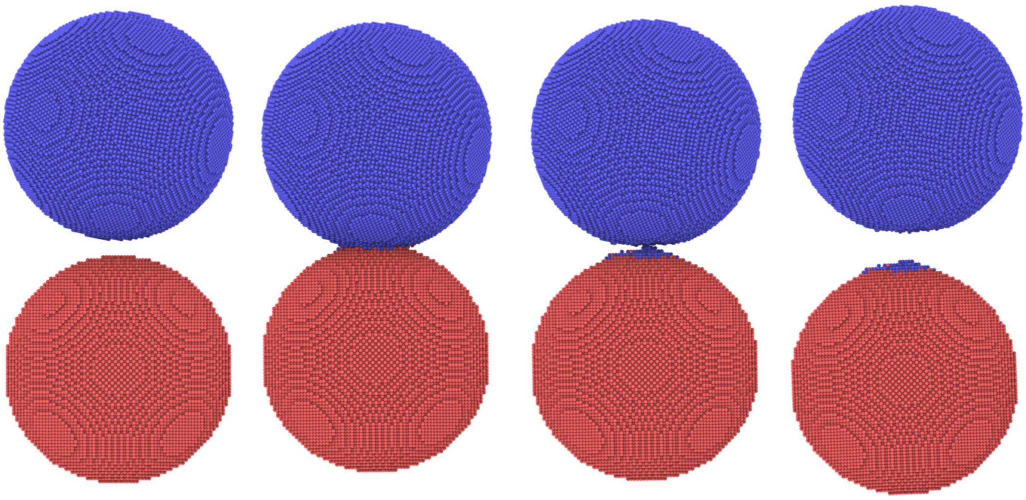

FIG. 6. Sequence of snapshots showing bouncing of the two NPs. Radius $R = 28.7$, $N = 10^5$, velocity $v = 0.2$.

collisions occur at values close to the maximum impact parameter. We show in Fig. 7 how the impact parameter influences the plasticity formation. Except for the lowest velocity $v = 0.3$—which is still below the critical velocity—we observe the clear trend that defect formation is maximum for central collisions and monotonically decreases with increasing impact parameter. This decrease is due to the fact that less volume is involved in the collision at large b.

This is shown in Fig. 8, where we see the plasticity resulting from a glancing collision. We use a high velocity, $v = 3$, since the number of defects formed at glancing incidence is small. The two NPs shear material off each other such that material is mixed between the two NPs. Despite the high velocity, only one NP received internal damage, in the form of plasticity. Note the simplicity of the resulting defect structure.

We note that at smaller velocities, the usual result is sticking of the 2 NPs, resulting in a NP-dimer rotating at high angular velocity but with no or only little internal defect creation.

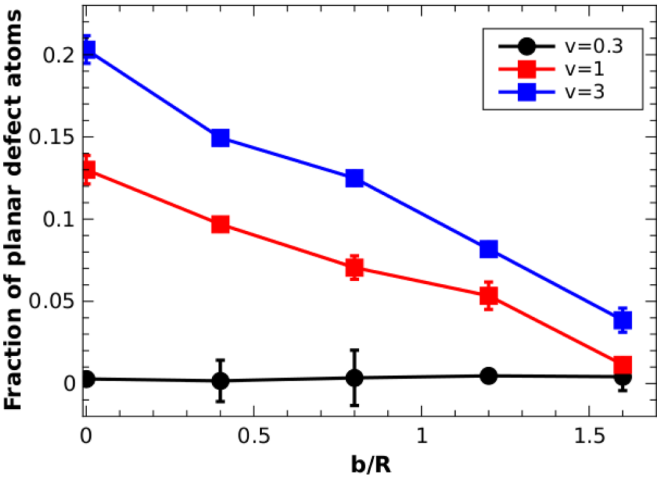

FIG. 7. Fraction of defect atoms after collision of 2 NPs with radius $R = 10.4$, $N = 5000$, as a function of impact parameter b. Data are provided for various velocities v.

F. Velocity dependence

Figure 9 assembles the information on the production of atoms in planar defects as a function of velocity for various radii studied. The data have been grouped for smaller ($N \leqslant 2\times10^4$, $R \leqslant 16.6$) and larger ($N \geqslant 3\times10^4$, $R \geqslant 18.9$) clusters in order to increase the readability of the plots. The picture for the larger NPs is clear: While at small velocities the number of defects formed is at the noise level (below 1 per mille), it increases steeply in a short range of velocities and reaches saturation values of around 0.05 or above at high velocities. The range of steep increase allows us to define the critical velocity of the elastic-plastic transition, which will be discussed in detail in Sec. III I. Its definition is, of course, prone to some arbitrariness, since the transition occurs smoothly in a velocity window. We shall use a fraction of 0.005 to determine v_c quantitatively. Figure 9(a) demonstrates that v_c monotonically decreases with increasing NP size.

The situation is somewhat less transparent at small NP sizes, Fig. 9(b). Here the "noise level" at small velocities strongly increases, since the number of atoms involved is small. However, one can still discern the trend that with decreasing NP size, the critical velocity increases, at least as long as $N \geqslant 5\times10^3$, $R \geqslant 10.4$. For even smaller clusters, we use a fraction of 0.05 to determine v_c quantitatively.

G. Statistics

The plasticity features shown here are typical of those developing; however, a large variety exists in the number of defects occurring in an individual collision event. It is caused by the different crystalline orientations of the two colliding NPs. Figure 10 shows this variety for several selected cases.

Figures 10(a) and 10(b) show the defect probability distribution for collisions in the vicinity of the critical velocity. We see a bimodal distribution, where either around 800 or around 0–100 defect atoms are created. At the smaller velocity, $v = 0.45$, the maximum for no defect generation is still dominant, but at the somewhat higher velocity of $v = 0.5$, the generation of plasticity (with around 800 atoms) takes over. Note that for the higher velocity also the number

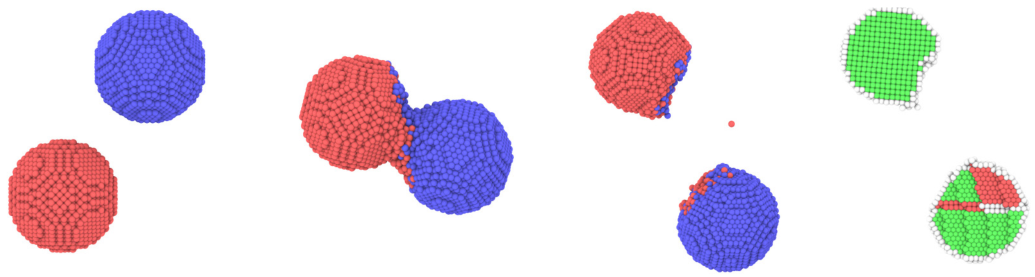

(a) (b) (c) (d)

FIG. 8. Typical example of defects generated at glancing incidence. Data are for the collision of two NPs of radius $R = 10.4$, $N = 5000$, colliding with velocity $v = 3$ at impact parameter $b/R = 1.6$. Panels (a)–(c) provide a time sequence of snapshots, where colors distinguish material from the two NPs. Panel (d) shows the defects formed inside the 2 NPs. Green: Undisturbed lattice; red: SF.

of high-damage events becomes more pronounced. At both velocities the average of these distributions—493 (783) defect atoms for $v = 0.45$ (0.5)—is actually rarely realized. Note, however, the strong increase (by around 60%) in the average defect number at the small velocity increase of 10%; this is the sign that we are around the critical velocity. This figure shows that the creation of plasticity in NP collisions sensitively depends on the NP orientation, in particular, in the vicinity of the critical velocity. This is also true of the energy dissipated in defect creation.

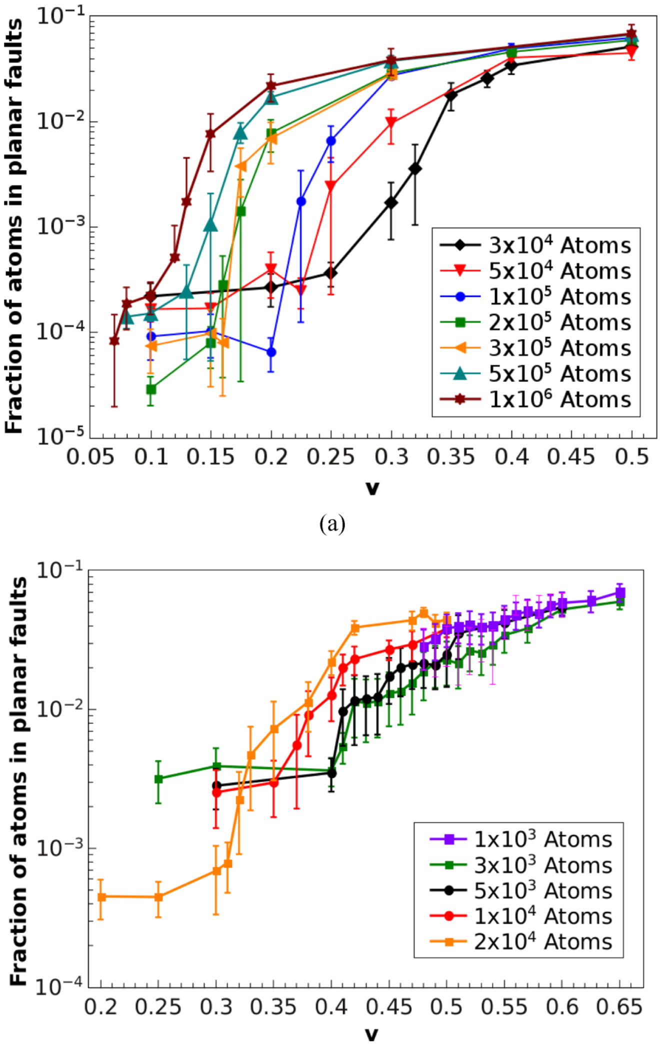

(a)

(b)

FIG. 9. Fraction of defect atoms created in central collisions as a function of collision velocity v. Data are for various NP sizes characterized by the number of atoms N in one NP.

Figure 10(c) shows the probability distribution for a collision scenario far above the critical velocity. It is approximately Gaussian distributed around the mean value of 12 297 with a standard deviation of 31%. It shows that while above the critical velocity, the creation of plasticity is the rule—no cases of 0 damage are seen in this figure—still the variation in relative orientations of the NPs with respect to each other leads to a wide variation in dislocation production in the individual cases.

H. Size dependence

While up to now we focused on the velocity dependence of the plasticity generation, Fig. 11 shows the evolution of the number of defects as a function of the NP size. At the largest velocity chosen here, $v = 0.5$ (far above the critical velocity for large spheres), we see that the relative number of defect atoms saturates for large spheres at a value of around 7%. Note that we observe *planar defects*, thus one might have assumed that the number of defect atoms evolves as R^2. But since the data in this plot have been normalized to the total number of atoms N, the MD data reveal that the number of defects increases as R^3, if the velocity is above the critical velocity.

The smallest velocity, $v = 0.2$, is still below the critical velocity for small NPs; hence virtually no plasticity is generated for $R \leqslant 30$. For larger NPs, the volume fraction of planar defects slowly increases. It must be assumed that it reaches a saturation level, however, only for considerably larger NPs than those investigated here. The velocity of $v = 0.3$ shows a behavior that is intermediate between the two other velocities studied.

I. The elastic-plastic threshold

The statistics of our simulation results allows us to determine the critical velocity v_c. We used the criterion that a collision is considered to result in plasticity if the fraction of defect atoms is above 0.5% of the total number of atoms in

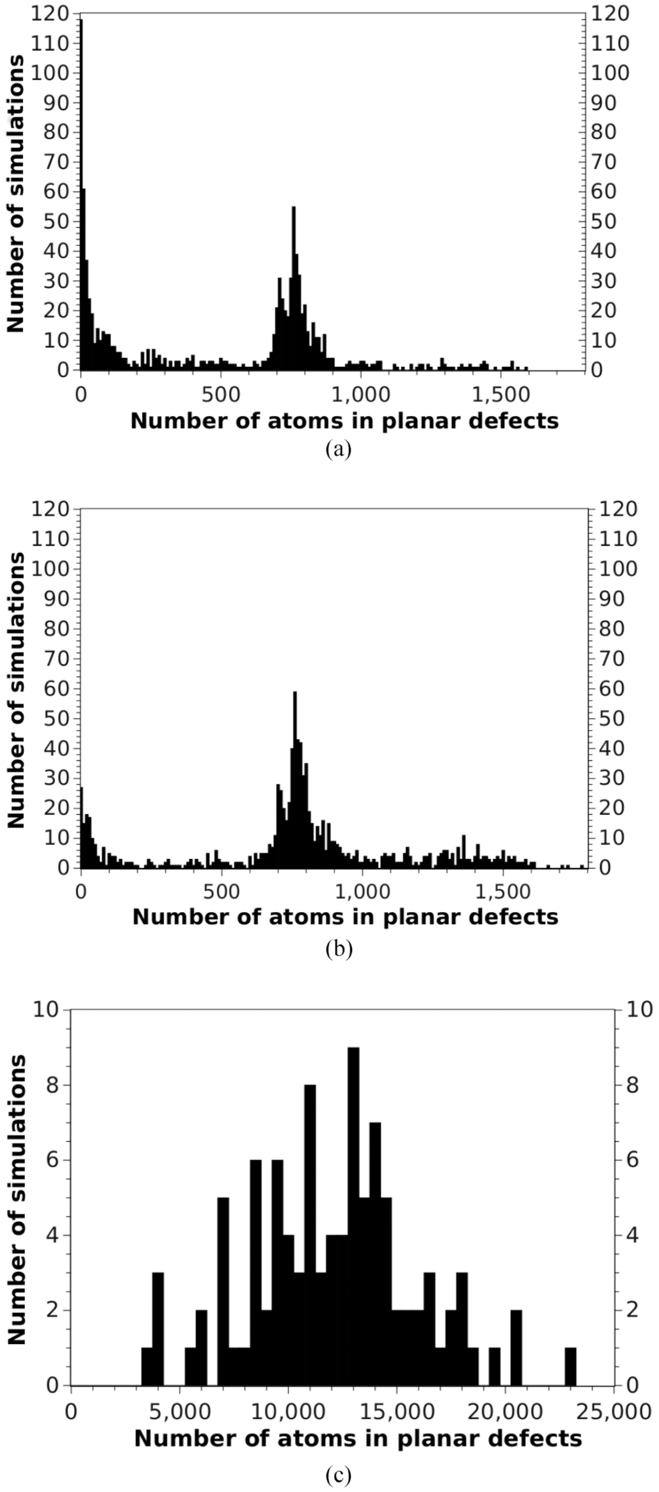

(a)

(b)

(c)

FIG. 10. Statistics of defect generation shows bimodal distribution for collisions of $N = 10^4$ NPs, $R = 13.2$, with $v = 0.45$ (a), which shift towards higher defect production at $v = 0.5$ (b). Far above the plasticity threshold ($N = 10^5$, $R = 28.7$, with $v = 0.5$) the distribution becomes unimodal (c).

the NPs; only for the two smallest cluster sizes used here, $N < 5000$, was a threshold of 5% used instead. The data shown in Fig. 12 exhibit a clear size dependence of the critical velocity [15].

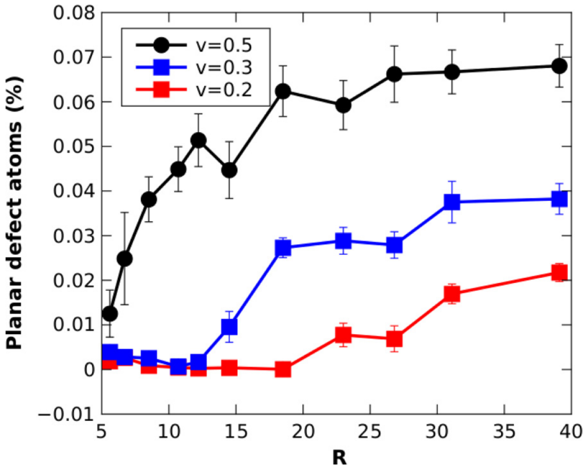

FIG. 11. Relative number of atoms contained in SFs as a function of the NP size, R. Data are for various collision velocities v.

An early model assumes v_c to be independent of the NP size; for two equal spheres it predicts [11–14]

$$v_c = 10.06\sqrt{\frac{Y^5}{E_{\rm ind}^4\rho}}, \tag{6}$$

where Y is the yield stress, $E_{\rm ind} = E/(1-\nu^2)$ is the indentation modulus, E and ν are Young's modulus and Poisson ratio for the material assumed to be isotropic, and ρ is the mass density. For a LJ material and assuming $Y = G/10 = 4$ for a defect-free single crystal [59], Eq. (6) gives $v_c = 0.027$. This value is far below our MD results.

Recently, the size dependence of v_c has been explained using the so-called *modified source model* [15]. It assumes that dislocations are formed in the contact zone of radius a; similarly to the idea behind a Frank-read source [54,60], the dislocations are emitted from the contact zone into the NP if the applied stress is larger than

$$p_c = \alpha\frac{Gb}{a}. \tag{7}$$

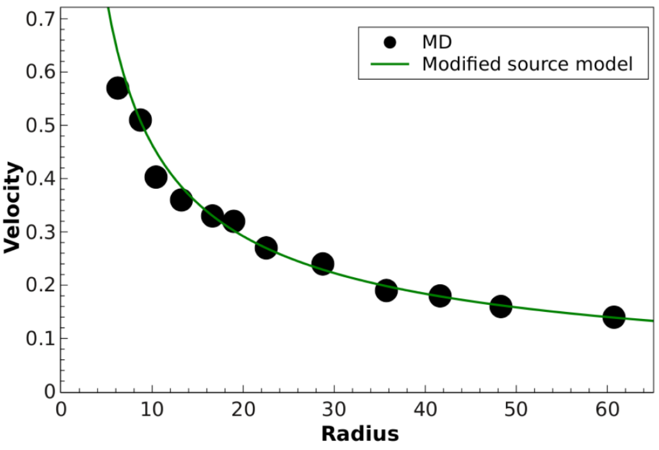

FIG. 12. Plastic threshold velocity, v_c, as a function of NP radius, R. Symbols: Our MD data. Line gives the modified source model, Eq. (9).

Here b denotes the Burgers vector and α is a prefactor in the range of 0.25–1 [61,62]; we use here $\alpha = 0.4$.

The pressure in the contact zone can be estimated from the Hugoniot relation

$$p = \rho v c_l = 11.41 v, \tag{8}$$

where the density ρ and longitudinal velocity of sound c_l for a LJ solid have been inserted to obtain the latter equality.

Using finally the $R^{2/3}$ dependence of the contact radius a, Eq. (4), the nucleation pressure is obtained from Eq. (7) as $p_c = 16.4/R^{2/3}$ and the critical velocity follows as

$$v_c = \frac{1.43}{R^{2/3}}. \tag{9}$$

Figure 12 demonstrates that this law describes our MD data surprisingly well.

In the past, the size dependence of NP collisions has been studied for other quantities than the elastic-plastic threshold. In particular, the rebound velocity, v_r, was investigated, which measures the minimum velocity necessary for NPs to bounce off each other; at lower velocities they stick. The rebound velocity is thought to be related to the critical velocity for plastic failure. Rennecke and Weber [63] measured v_r for Ag NPs and showed an increase with decreasing particle radius R. The model by Weir and McGavin [64] assumes rebound to occur on complete plastic failure and predicts $v_r \propto 1/R$. Using MD simulations of Cu NP collisions, Han *et al.* [53] showed that the onset of plasticity is shifted to higher velocities for smaller NPs. Eventually, Takato *et al.* [35] determined a so-called yield velocity v_y as the velocity, above which the rebound velocity stays constant; their simulations on LJ NPs gave $v_y \propto R^{-0.65}$. We conclude that the modified source model [15] provides a transparent explanation for the $R^{-2/3}$ decrease of the threshold for plasticity in NP collisions, which is related to the decrease of the rebound velocity and the yield velocities discussed above.

Finally, we note that quasistatic compression experiments were used to determine a size dependence for the onset of plastic deformation. Mordehai *et al.* [21] studied dislocation nucleation in Au NPs under quasistatic compression. Experiments performed on $R = 100$–500 nm sized NPs showed a decrease of the critical stress for the onset of plastic deformation as a power law, $\sigma_c \propto R^{-n}$ with $n = 0.77 \pm 0.16$. Accompanying MD simulations were performed in the size range of $R = 3$–12 nm and gave a similar power law with $n = 0.74 \pm 0.08$; here the NPs were compressed perpendicular to $\{111\}$ faces with a velocity of $v = 1$ m/s. The authors explained their findings by regression to the well-known dependence of the critical stress needed to nucleate a dislocation loop [65]

$$\sigma_c = \frac{Gb}{2\pi r_c}, \tag{10}$$

where r_c is the critical radius of the loop beyond which the work done by the applied stress on loop expansion exceeds the elastic energy of the dislocation, and the loop will grow. The authors expanded this model by assuming that the elastic stress created during compression is inhomogeneous in the NP; it is highest near the vertices of the faceted NP and decays along the slip planes with distance r from the NP vertices with a power-law $\sigma(r) \propto (R/r)^n$ where the power-law exponent n is motivated by elastic theory [66] but is left as a free fitting factor. Using crystal-elasticity finite-element-method simulations of an $R = 500$ nm NP, the power-law decay is determined as $n = 0.74 \pm 0.08$. The extension of Eq. (10) to a spatially varying stress field leads to

$$\sigma_c \propto \frac{1}{R^n}. \tag{11}$$

Thus this study [21] relates the size dependence of NP to the inhomogeneous stress distribution inside a uniaxially compressed faceted NP.

IV. SUMMARY

Low-velocity collisions are elastic in the sense that no defects in the NP bulk are formed. However, due to the strong mutual attraction, the two NPs merge at a circular contact interface. Pressure and contact radius undergo a series of damped oscillations. At higher velocities, planar defects (SFs and nanotwins) are generated. Close to the elastic-plastic threshold, these are generated as isolated planar defects; while they nucleate at the interface they propagate through the entire NP. The generation of SFs is the characteristic result of the NP plasticity studied here. The large stress in the contact area leads to partial dislocations traveling rapidly through the material. When they reach the opposite surface of the NP, they are absorbed, leaving behind the SF. If several SFs are produced in consecutive planes, a nanotwin is formed.

With increasing velocity, also heterogeneous nucleation at the vacuum surface of the NPs is observed. The density of defects increases such that the number of defect atoms becomes proportional to the total number of atoms; even though the defects are generated as planar faults, their volume fraction saturates (at around 7%).

Plasticity is generated above a critical velocity, v_c. It was recently found [15] that in contrast to the widely used assumption that v_c is size independent, the critical velocity increases as $R^{-2/3}$ for small NP radii R. This increase is caused by the dynamics of the dislocations generated in the contact zone: In order to emit dislocations from this zone into the NP, a stress is necessary which depends inversely on the contact zone radius, a, according to the line tension of the dislocation described as for a simple (Frank-Read) source. We find here that the dependence of $a \propto R^{2/3}$ valid for adhesive contacts models well the $R^{-2/3}$ dependence of the critical velocity.

Close to threshold, plasticity is subject to large fluctuations, since different NP orientations will react differently to the pressure developing in the collision. A statistics made over many orientations shows a bimodal distribution of the number of defects, which shows a peak at zero defects (purely elastic collision) besides an additional peak due to a planar defect spanning one of the NPs. A reliable estimate of the critical velocity can only be made after averaging over many orientations.

This study focused on the collision behavior of NPs with a simplified shape and structure: spherical NPs with a single-crystalline fcc structure. Future investigations might extend the present results to include the influence of pre-existing defects in these NPs—in particular grain and twin boundaries. In addition, it will be interesting to study the effect of a faceted surface, such as it will be acquired by NPs close to equilibrium. Finally, real NPs may be amorphous; the deformation behavior of such particles cannot be described by the generation of dislocations as for crystalline particles. The analysis of the velocity dependence of amorphous NPs needs hence be based either on macroscopic concepts such as the energy dissipation during the collision (the coefficient of restitution), on geometric parameters describing the overall deformation of the NPs, or on the characterization of specific deformation features existing in the amorphous state, i.e., shear bands.

ACKNOWLEDGMENTS

E.M., D.T., and E.M.B. acknowledge support from SeCTyP-UNCuyo Grant No. M003 and ANPCyT Grant No. PICT-2014-0696. E.M. and D.T. acknowledge support from CONICET. H.M.U. was supported by the Deutsche Forschungsgemeinschaft via Sonderforschungsbereich 926.

[1] E. Grün, in *Encyclopedia of the Solar System*, 2nd ed., edited by L. A. McFadden, P. R. Weissman, and T. V. Johnson (Academic Press, New York, 2007), p. 621.

[2] M. Jutzi, W. Benz, and P. Michel, Icarus **198**, 242 (2008).

[3] B. K. Mishra and C. Thornton, Int. J. Miner. Process. **61**, 225 (2001).

[4] G. K. Reynolds, J. S. Fu, Y. S. Cheong, M. J. Hounslow, and A. D. Salman, Chem. Eng. Sci. **60**, 3969 (2005).

[5] H. A. Carmona, F. K. Wittel, F. Kun, and H. J. Herrmann, Phys. Rev. E **77**, 051302 (2008).

[6] Z. B. Tong, R. Y. Yang, A. B. Yu, S. Adi, and H. K. Chan, Powder Technol. **196**, 213 (2009).

[7] J. Duran, *Sands, Powders, and Grains: An Introduction to the Physics of Granular Materials* (Springer-Verlag, Berlin, 2000).

[8] T. Pöschel and T. Schwager, *Computational Granular Dynamics: Models and Algorithms* (Springer, Berlin, 2005).

[9] S. Krijt, C. Güttler, D. Heißelmann, C. Dominik, and A. G. G. M. Tielens, J. Phys. D **46**, 435303 (2013).

[10] C. Dominik and A. G. G. M. Tielens, Astrophys. J. **480**, 647 (1997).

[11] R. M. Davies, Proc. R. Soc. London A **197**, 416 (1949).

[12] K. L. Johnson, *Contact Mechanics* (Cambridge University Press, Cambridge, 1985).

[13] A. Chokshi, A. G. G. M. Tielens, and D. Hollenbach, Astrophys. J. **407**, 806 (1993).

[14] C. Thornton and Z. Ning, Powder Technol. **99**, 154 (1998).

[15] E. N. Millán, D. R. Tramontina, H. M. Urbassek, and E. M. Bringa, Phys. Chem. Chem. Phys. **18**, 3423 (2016).

[16] L. M. Hale, D.-B. Zhang, X. Zhou, J. A. Zimmerman, N. R. Moody, T. Dumitrica, R. Ballarini, and W. W. Gerberich, Comput. Mater. Sci. **54**, 280 (2012).

[17] A. Tolvanen and K. Albe, Beilstein J. Nanotechnol. **4**, 173 (2013).

[18] D. Jang, X. Li, H. Gao, and J. R. Greer, Nat. Nanotechnol. **7**, 594 (2012).

[19] N. Pradeep, D.-I. Kim, J. Grobelny, T. Hawa, B. Henz, and M. R. Zachariah, Appl. Phys. Lett. **91**, 203114 (2007).

[20] W.-Z. Han, L. Huang, S. Ogata, H. Kimizuka, Z.-C. Yang, C. Weinberger, Q.-J. Li, B.-Y. Liu, X.-X. Zhang, J. Li *et al.*, Adv. Mater. **27**, 3385 (2015).

[21] D. Mordehai, S.-W. Lee, B. Backes, D. J. Srolovitz, W. D. Nix, and E. Rabkin, Acta Mater. **59**, 5202 (2011).

[22] F. F. Abraham, D. Brodbeck, R. A. Rafey, and W. E. Rudge, Phys. Rev. Lett. **73**, 272 (1994).

[23] F. F. Abraham, D. Schneider, B. Land, D. Lifka, J. Skovira, J. Gerner, and M. Rosenkrantz, J. Mech. Phys. Sol. **45**, 1461 (1997).

[24] F. F. Abraham, Europhys. Lett. **38**, 103 (1997).

[25] B. L. Holian and P. S. Lomdahl, Science **280**, 2085 (1998).

[26] T. Hatano, Phys. Rev. Lett. **93**, 085501 (2004).

[27] D. Tanguy, M. Mareschal, P. S. Lomdahl, T. C. Germann, B. L. Holian, and R. Ravelo, Phys. Rev. B **68**, 144111 (2003).

[28] J. A. Zimmerman, H. Gao, and F. F. Abraham, Modell. Simul. Mater. Sci. Eng. **8**, 103 (2000).

[29] F. Baletto and R. Ferrando, Rev. Mod. Phys. **77**, 371 (2005).

[30] J. Wang, F. Sansoz, J. Huang, Y. Liu, S. Sun, Z. Zhang, and S. X. Mao, Nat. Commun. **4**, 1742 (2013).

[31] M. Kalweit and D. Drikakis, Phys. Rev. B **74**, 235415 (2006).

[32] H. Kuninaka and H. Hayakawa, Phys. Rev. E **79**, 031309 (2009).

[33] H. Tanaka, K. Wada, T. Suyama, and S. Okuzumi, Prog. Theor. Phys. Suppl. **195**, 101 (2012).

[34] S.-C. Jung, J.-G. Bang, and W.-s. Yoon, J. Aerosol Sci. **50**, 26 (2012).

[35] Y. Takato, S. Sen, and J. B. Lechman, Phys. Rev. E **89**, 033308 (2014).

[36] A. Michels, H. Wijker, and H. K. Wijker, Physica **15**, 627 (1949).

[37] J.-P. Hansen and L. Verlet, Phys. Rev. **184**, 151 (1969).

[38] T. Halicioglu and G. M. Pound, Phys. Status Solidi A **30**, 619 (1975).

[39] S. Plimpton, J. Comput. Phys. **117**, 1 (1995).

[40] A. Stukowski and K. Albe, Model. Simul. Mater. Sci. Eng. **18**, 085001 (2010).

[41] A. Stukowski, V. V. Bulatov, and A. Arsenlis, Model. Simul. Mater. Sci. Eng. **20**, 085007 (2012).

[42] A. Stukowski, Model. Simul. Mater. Sci. Eng. **20**, 045021 (2012).

[43] W. Humphrey, A. Dalke, and K. Schulten, J. Mol. Graphics **14**, 33 (1996).

[44] A. Stukowski, Model. Simul. Mater. Sci. Eng. **18**, 015012 (2010).

[45] D. J. Quesnel, D. S. Rimai, and L. P. DeMejo, Phys. Rev. B **48**, 6795 (1993).

[46] D. W. Brenner and B. J. Garrison, Phys. Rev. B **34**, 5782 (1986).

[47] M. Vergeles, A. Maritan, J. Koplik, and J. R. Banavar, Phys. Rev. E **56**, 2626 (1997).

[48] C. Anders, S. Meßlinger, and H. M. Urbassek, Surf. Sci. **600**, 2587 (2006).

[49] D. Maugis, *Contact, Adhesion and Rupture of Elastic Solids* (Springer, Berlin, 2000).

[50] B. Luan and M. O. Robbins, Nature **435**, 929 (2005).
[51] B. Luan and M. O. Robbins, Phys. Rev. E **74**, 026111 (2006).
[52] N. Ohnishi, E. M. Bringa, B. A. Remington, G. Gilmer, R. Minich, Y. Yamaguchi, and A. G. G. M. Tielens, J. Phys.: Conf. Ser. **112**, 042017 (2008).
[53] L. B. Han, Q. An, S. N. Luo, and W. A. Goddard III, Mater. Lett. **64**, 2230 (2010).
[54] J. P. Hirth and J. Lothe, *Theory of Dislocations*, 2nd ed. (Wiley, New York, 1982).
[55] A. Hunter, R. F. Zhang, I. J. Beyerlein, T. C. Germann, and M. Koslowski, Model. Simul. Mater. Sci. Eng. **21**, 025015 (2013).
[56] G. Ziegenhain, A. Hartmaier, and H. M. Urbassek, J. Mech. Phys. Sol. **57**, 1514 (2009).
[57] Y. Kogure, T. Tsuchiya, and Y. Hiki, J. Phys. Soc. Jpn. **56**, 989 (1987).
[58] M. Suri and T. Dumitrica, Phys. Rev. B **78**, 081405 (2008).
[59] A. Kelly and N. H. Macmillan, *Strong Solids*, 3rd ed. (Clarendon Press, Oxford, 1986).
[60] M. A. Meyers and K. K. Chawla, *Mechanical Behavior of Materials*, 2nd ed. (Cambridge University Press, Cambridge, 2010).
[61] V. B. Shenoy, R. V. Kukta, and R. Phillips, Phys. Rev. Lett. **84**, 1491 (2000).
[62] A. K. Nair, E. Parker, P. Gaudreau, D. Farkas, and R. D. Kriz, Int. J. Plast. **24**, 2016 (2008).
[63] S. Rennecke and A. P. Weber, J. Aerosol Sci. **58**, 135 (2013).
[64] G. Weir and P. McGavin, Proc. R. Soc. London. Ser. A **464**, 1295 (2008).
[65] D. Hull and D. J. Bacon, *Introduction to Dislocations*, 3rd ed. (Pergamon, Oxford, 1984).
[66] M. Paggi and A. Carpinteri, Appl. Mech. Rev. **61**, 020801 (2008).